FRONTIERS OF PHYSICS

RESEARCH ARTICLE
Volume 18 / Issue 4 / 43301 / 2023

Two-dimensional rectangular bismuth bilayer: A novel dual topological insulator

Shengshi Li[1,†], Weixiao Ji[1], Jianping Zhang[1], Yaping Wang[2,‡], Changwen Zhang[1], Shishen Yan[1]

1 Spintronics Institute, School of Physics and Technology, University of Jinan, Jinan 250022, China
2 State Key Lab of Crystal Materials and Institute of Crystal Materials, Shandong University, Jinan 250100, China
Corresponding authors. E-mail: †sdy_liss@ujn.edu.cn, ‡wangyaping1003@163.com
Received November 7, 2022; accepted January 15, 2023

ABSTRACT

Dual topological insulator (DTI), which simultaneously hosts topological insulator (TI) and topological crystalline insulator (TCI) phases, has attracted extensive attention since it has a better robustness of topological nature and broad application prospects in spintronics. However, the realization of DTI phase in two-dimensional (2D) system is extremely scarce. By first-principles calculations, we predict that the 2D rectangular bismuth (R–Bi) bilayer is a novel DTI, featured by $\mathbb{Z}_2$ topological invariant $\mathbb{Z}_2 = 1$, mirror Chern number $C_M = -1$, and metallic edge states within the bulk band gap. More interestingly, the TCI phase in bilayer is protected by horizontal glide mirror symmetries, rather than the usual mirror symmetry. The bulk band gap can be effectively tuned by vertical electric field and strain. Besides, the electric field can trigger the transition between TI and metallic phases for the bilayer, accompanied by the annihilation of TCI phase. On this basis, a topological field effect transistor is proposed, which can rapidly manipulate spin and charge carriers via electric field. The KBr(110) surface is demonstrated as an ideal substrate for the deposition of bilayer. These findings provide not only a new strategy for exploiting 2D DTI, but also a promising candidate for spintronic applications.

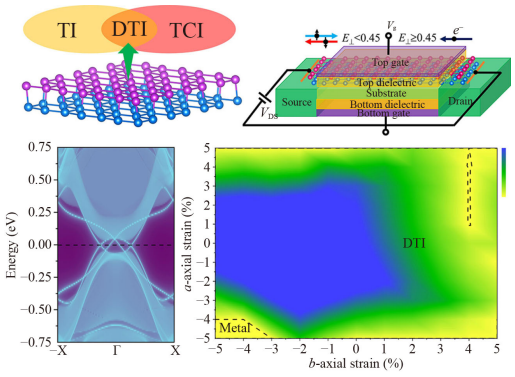

Keywords dual topological insulator, Bi bilayer, glide mirror symmetry, first-principles calculations

1 Introduction

In the past few decades, topological quantum state has become one of the most active and important research fields in condensed matter physics. Hitherto, various topological materials have been proposed and explored intensely, such as topological insulator (TI) and topological crystalline insulators (TCI) [1–5]. The unique hallmark of TI and TCI is the presence of metallic edge/surface states with Dirac dispersions inside of the insulating bulk state, which endows them with great application potential in spintronics. The TI phase with the protection of time-reversal ($\mathcal{T}$) symmetry is featured with a nonzero $\mathbb{Z}_2$ topological invariant. While the TCI phase, which is commonly protected by mirror ($\mathcal{M}$) symmetries, is characterized by a nonzero mirror Chern number C_M. Recently, the blend of TI and TCI phases has received considerable interest, which gives rise to a new class of topological material, named as dual topological insulator (DTI) [6–15]. The topological state in DTI is simultaneously protected by $\mathcal{T}$ and $\mathcal{M}$ symmetries, thus rendering a superior robustness of metallic edge/surface states against perturbation. In other words, the individual $\mathcal{T}$ ($\mathcal{M}$) symmetry breaking would not affect the edge/

https://doi.org/10.1007/s11467-023-1262-x

surface states protected by the $\mathcal{M}$ ($\mathcal{T}$) symmetry. Such characteristic enables the separate control of these two topological phases, which is advantageous to design spintronic devices with stable performance. To date, the research of three-dimensional (3D) DTI has made certain progress in both theory and experiment [8–15]. By comparison, only a minority of two-dimensional (2D) DTIs have been proposed, including Na_3Bi [6], Na_2MgPb [7], and Na_2CdSn [7], and they are still confined to theoretical prediction without experimental evidence. It is noteworthy that the TCI phases in these 2D DTIs are all protected by the mirror symmetry $\mathcal{M}_z$ ($z \to -z$). In fact, as an alternative mechanism, the glide mirror symmetry also plays a pivotal role in protecting TCI phase [16–19], but it has been scarcely studied in 2D DTI. Therefore, the realization of 2D DTI with protections of T and glide mirror symmetries is of great interest and importance, which can not only broaden the scope of DTI but also provide excellent candidates for device applications.

As is known to all, the emergence of topological quantum state is closely associated with the spin–orbit coupling (SOC). Bismuth (Bi), as a "heavy" element with sizable SOC, has attracted widespread attention. Many Bi-containing solids have been verified to harbor exotic topological phenomena, such as TI phase [20–23], DTI phase [6, 10, 13–15], and quantum anomalous Hall (QAH) effect [24]. Meanwhile, the Bi(111) and Bi(110) films have been experimentally demonstrated as 2D TIs [25, 26], the so-called quantum spin Hall (QSH) insulators, whose conductive edge states can be detected directly. Due to the distinctive electronic situation, Bi shows very rich crystal chemistry, and a variety of 2D bismuthic films with nontrivial topology are proposed [27–30]. Nevertheless, the DTI phase has not yet been discovered in these reported Bi elemental films. In this work, using first-principles calculations, we predict that the 2D rectangular bismuth (R–Bi) bilayer can realize the long-sought DTI phase. Such topologically nontrivial state is characterized by $\mathbb{Z}_2$ topological invariant $\mathbb{Z}_2 = 1$, mirror Chern number $C_M = -1$, and metallic edge states across the bulk band gap. Remarkably, the TCI phase in R–Bi bilayer is protected by horizontal glide mirror symmetries, instead of the conventional mirror symmetry. The tunability of bulk band gap is achievable through vertical electric field and strains. More interestingly, the electric field can drive the R–Bi bilayer to convert between QSH insulator and metal, which allows the rapid switch between spin and charge carriers, and thus a topological field effect transistor (TFET) is proposed based on the R–Bi bilayer. Besides, the TI phase can be preserved when the R–Bi bilayer is deposited on the KBr(110) surface. These results offer a good platform for investigating intriguing topological quantum state and developing innovative spintronic devices.

2 Computational details

All first-principles calculations were performed using the Vienna *ab initio* simulation package (VASP) [31, 32], which is based on density-functional theory (DFT). The projector-augmented-wave (PAW) method was employed to describe the ionic potential [33]. The exchange–correction interaction was treated by the generalized gradient approximation (GGA) in the form of Perdew–Burke–Ernzerhof (PBE) functional [34, 35]. The lattice parameter and atom position were fully optimized until the force and energy were converged to 0.005 eV/Å and 10^{-5} eV. The energy cutoff of the plane waves was set to 400 eV. A 11 × 11 × 1 k-point sampling was used for the Brillouin zone integrations, and a vacuum region larger than 20 Å was adapted to avoid the interaction caused by periodic boundary conditions. The van der Waals (vdW) interaction in heterostructure was described by the DFT-D3 method [36, 37]. The *ab initio* molecule dynamic (AIMD) simulation was performed by using a 3 × 3 × 1 supercell at 300 K. The $\mathbb{Z}_2$ topological invariant was determined by the evolution of the Wannier center of charges (WCCs) method which was proposed by Soluyanov and Vanderbilt [38, 39], see Note 1 of the Supporting Information (SI). The calculation of C_M was implemented by the method presented in Note 2 of the SI.

3 Results

3.1 Geometric structure and stability of R–Bi bilayer

Figure 1(a) presents the top and side views of R–Bi bilayer. The unit cell of R–Bi bilayer consists of eight Bi atoms, exhibiting an orthorhombic lattice with the space group *Cmma* (No. 67). There is a relative displacement between two bismuthic layers, and each Bi atom covalently coordinates with four Bi atoms. After structural optimization, the lattice constants a and b are found to be 6.59 and 6.89 Å, respectively. Three types of Bi–Bi bond lengths are obtained, i.e., $d_1 = 3.07$ Å, $d_2 = 3.31$ Å, and $d_3 = 3.01$ Å. The thickness of R–Bi bilayer turns out to be 2.99 Å. To evaluate the structural stability of R–Bi bilayer, the formation energy is firstly calculated based on $E_f = [E(\text{R–Bi}) - 8\mu(\text{Bi})]/8$. Here, E(R–Bi) is the total energy of unit cell, and μ(Bi) is the chemical potential of Bi atom obtained from its stable bulk phase. The resultant E_f is –1.12 eV/atom, which is comparable to those of experimentally fabricated Bi(111) (–1.14 eV/atom) and Bi(110) (–1.13 eV/atom) films, as shown in Fig. S1 of the SI. Furthermore, the thermal stability of bilayer is examined by the AIMD simulation. As can be seen from Fig. S2 that the total energy fluctuates smoothly with increasing time, and neither structural deformation nor phase transformation can be observed during the simula-

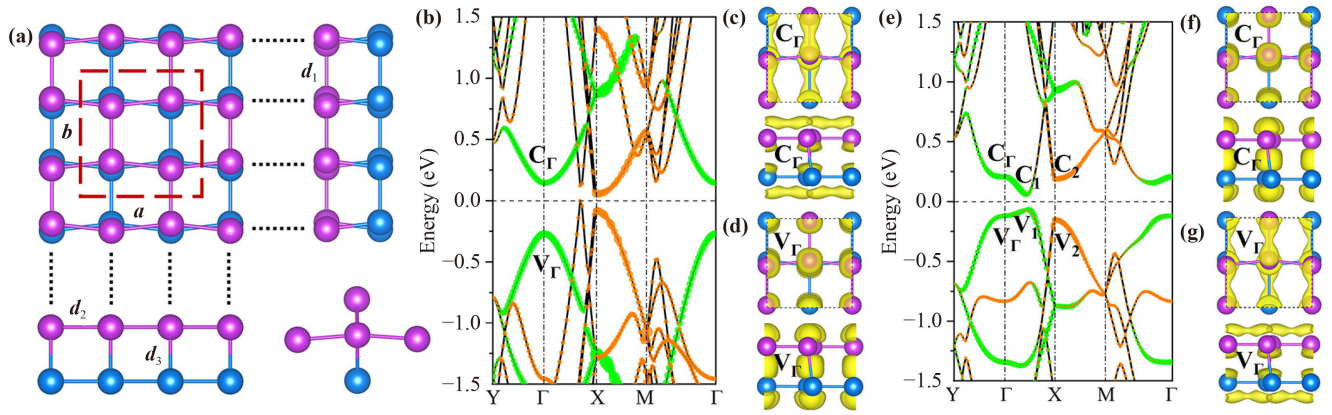

Fig. 1 **(a)** Top and side views, as well as bonding mode of R–Bi bilayer. The purple and bule balls represent upper and lower Bi atoms, respectively. **(b–d)** Orbital-resolved band structure without SOC and calculated charge density distributions of C_Γ and V_Γ. **(e, f)** Orbital-resolved band structure with SOC and calculated charge density distributions of C_Γ and V_Γ. The green and orange circles in (b) and (e) indicate p_z and $p_{x,y}$ orbitals, respectively.

tion, suggesting that such 2D system is thermally stable at room temperature. The above calculations indicate that the R–Bi bilayer is promising to be synthesized and stabilized in experiment.

3.2 Electronic and topological properties of R–Bi bilayer

Then the electronic property of R–Bi bilayer is explored. Figure 1(b) displays the orbital-resolved band structure without SOC, in which a semiconducting nature with an indirect band gap of 58.1 meV is obtained for the R–Bi bilayer. The conduction band minimum (CBM) and valence band maximum (VBM), which are dominated by Bi-$p_{x,y}$ orbitals, are located at the X point and the (0.35, 0.00, 0.00) point along the high-symmetry line Γ–X, respectively. While the electronic states near the Γ point are mainly contributed by Bi-p_z orbital. To visualize the p_z orbital contribution, the charge density distributions of C_Γ and V_Γ are calculated, as shown in Figs. 1(c) and (d). One can see that the charge densities of V_Γ and C_Γ are distributed at the interlayer Bi–Bi bonds and the bilayer surface, respectively, revealing the bonding and antibonding states of p_z orbital. When taking SOC into account, the band structure undergoes a dramatic change, especially for the electronic states nearest to the Fermi level in the vicinity of Γ point, see Fig. 1(e). The semiconductor property of R–Bi bilayer is maintained, but shows a direct band gap of 125.3 meV, with CBM (C_1) and VBM (V_1) both located along the high-symmetry line Γ–X. Interestingly, the charge density distributions of V_Γ and C_Γ are contrast to the results without considering SOC, as depicted in Figs. 1(f)–(g). In other word, the bonding and antibonding states of p_z orbital are inverted at the Γ point due to the SOC effect, suggesting the emergence of band inversion. To understand the change of band structure and such band inversion, evolutions of band structure and energy levels with regard to SOC strength ($\eta = \lambda/\lambda_0$, λ and λ_0 are artificial and actual SOC strength, respectively) are plotted in Fig. S3 and Fig. 2(a), respectively. With increasing η, the continuous shifts of lowermost conduction band and uppermost valence band determined by p_z orbital near the Γ point can be observed obviously. In addition, along the high-symmetry line Γ–X, two band crossings contributed by $p_{x,y}$ and p_z orbitals in valence and conduction bands are gapped, see Fig. S3, and the magnitude of band gap opening is proportional to the η. The change of band structure after considering SOC is resulted from these two phenomena. It should be noted that the other bulk bands shift slightly under the SOC effect. Subsequently, the η dependence of band inversion is analyzed. In Fig. 2(a), as the η is increased from zero, both V_Γ and C_Γ move towards the Fermi level, while the VBM and CBM exhibit contrary phenomenon, which makes the band gap enlarged until $\eta = 0.6$. For the case of $\eta = 0.7$, the V_Γ and C_Γ have become VBM and CBM, respectively. More importantly, the band gap undergoes a process of closing and reopening at the critical point of $\eta = 0.74$, implying the occurrence of band inversion and nontrivial topology in R–Bi bilayer.

To determine the topological property of R–Bi bilayer, we straightly calculate the $\mathbb{Z}_2$ topological invariant. Figure 2(b) displays the evolution of WCCs between two time-reversal invariant momenta, in which arbitrary horizontal reference line crosses it with odd times, indicating $\mathbb{Z}_2 = 1$. Besides, the edge states of a semi-infinite lattice constructed by an iterative Green's function method [40, 41] are also calculated based on the maximally localized Wannier functions (MLWFs). As illustrated in Fig. 2(c), three pairs of edge states that connect valence and conduction bands can be captured within the bulk band gap. In view of this, the R–Bi bilayer is an intrinsic QSH insulator. To give insight into the origin of the topological property, the evolution of atomic orbitals

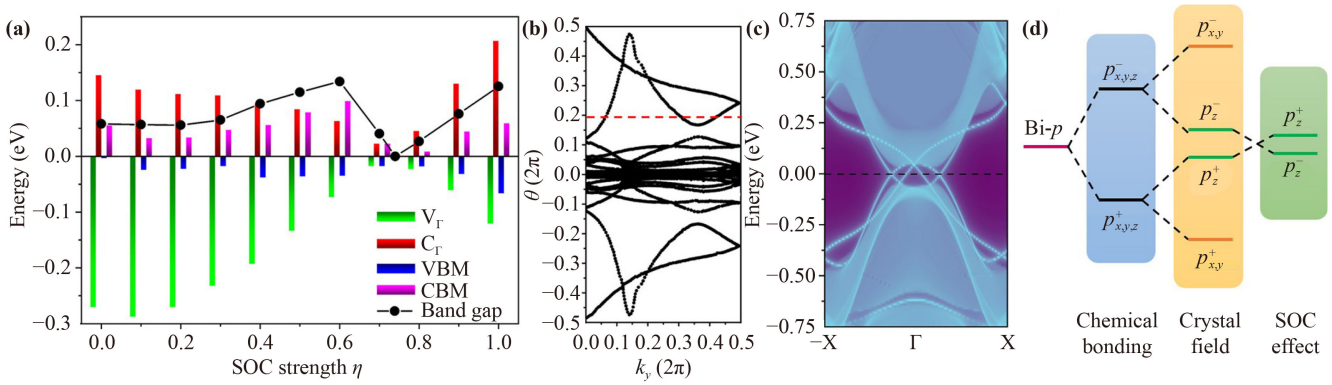

Fig. 2 **(a)** Variations of energy levels and band gap as a function of SOC strength η for R–Bi bilayer. **(b, c)** Calculated WCCs and edge states of R–Bi bilayer. **(d)** Evolution of atomic orbitals under chemical bonding, crystal field, and SOC effects.

near the Γ point are analyzed under the stages of chemical bonding, crystal field, and SOC effect, see Fig. 2(d). Here, the Bi-*s* orbital is neglected since the electronic states near the Fermi level are mainly contributed by the Bi-*p* orbitals. Firstly, the formation of Bi-Bi bond drives the *p* orbitals to split into bonding and antibonding states, i.e., $p^{+}_{x,y,z}$ and $p^{-}_{x,y,z}$. Under the effect of crystal field, the *p* orbitals would further split into in-plane $p_{x,y}$ and out-of-plane p_z orbitals, labeled as $p^{-}_{x,y}$, $p^{+}_{x,y}$, p^{-}_{z}, and p^{+}_{z}, in which the p^{-}_{z} is located above the p^{+}_{z}. When SOC is considered, the band inversion between p^{-}_{z} and p^{+}_{z} is generated near the Fermi level. Consequently, the topologically nontrivial phase in R–Bi bilayer is attributed to the joint action of crystal field and SOC effect.

Next, the η-dependent edge states of R–Bi bilayer are investigated, as shown in Fig. S4. For cases of $\eta = 0.3$ and $\eta = 0.6$, although the band inversion is absent, there are two pairs of edge states across the bulk band gap. The Fermi level crosses two times for the edge states between –X and Γ points. These even numbers of crossings indicate that the QSH phase has yet to arise. When the η is equal to 0.9, another pair of edge states is emerged in the middle. In this context, odd numbers of intersections between Fermi level and edge states are produced, revealing that the R–Bi bilayer harbors QSH effect. It is remarkable that the preexisting two pairs of edge states are mirror symmetric with respect to the Γ point, which is very similar to the characteristic of edge states of TCI. The C_{M} of R–Bi bilayer is therefore calculated and the result shows $C_{\mathrm{M}} = -1$, evidencing that the R–Bi bilayer also has the TCI phase. Considering the established TI phase, the R–Bi bilayer belongs to a typical 2D DTI. In terms of the edge states, the pair in the middle is contributed by the QSH effect, while the two pairs located on both sides are yielded by the TCI phase. Additionally, the obtained C_{M} for R–Bi bilayer is distinctly different from that in previous reported 2D TCIs ($C_{\mathrm{M}} = -2$) [42–44]. As mentioned above, the TCI phase in a 2D DTI is generally protected by the mirror symmetry M_z. For R–Bi bilayer, the space group *Cmma* totally contains six mirror symmetry operations, i.e., two vertical mirror symmetries M_x and M_y, two vertical glide mirror symmetries $\mathcal{G}_x$ and $\mathcal{G}_y$, and two horizontal glide mirror symmetries ${\mathcal{G}_z}^a$ ($\{M_z|\frac{1}{2}\,0\}$) and ${\mathcal{G}_z}^b$ ($\{M_z|0\,\frac{1}{2}\}$), see Figs. S5(a) and (b). It is notable that the $\mathcal{M}_z$ is absent intrinsically. Thereby, the TCI phase in R–Bi bilayer is most probably protected by ${\mathcal{G}_z}^a$ and ${\mathcal{G}_z}^b$, since they are the only ones that have the horizontal mirror operation. To verify this hypothesis, two horizontal glide mirror symmetry breaking operations are implemented by artificially driving two Bi atoms to deviate from their equilibrium positions, as shown in Figs. S5(c)–(h). When only the ${\mathcal{G}_z}^a$ is broken, the edge states along the *a* direction contributed by the TCI phase have been preserved intactly, whereas the edge states along the *b* direction are separated by a band gap, see Figs. S5(c)–(e). On the other hand, for the breaking of ${\mathcal{G}_z}^b$, the edge states along the *a* direction are disconnected with valence and conduction bands although they are existent inside of the bulk band gap, while the edge states along the *b* direction are immune to such symmetry breaking, as depicted in Figs. S5(f)–(h). Thus, the TCI phase in R–Bi bilayer is jointly protected by ${\mathcal{G}_z}^a$ and ${\mathcal{G}_z}^b$, which are responsible for edge states of different boundaries, respectively. Beyond that, the edge states derived from the QSH effect are maintained, which indicates that the TI phase is robust against the structural perturbation. The dual topological character provides more opportunities for R–Bi bilayer to be utilized in spintronic devices.

3.3 Effect of vertical electric field on R–Bi bilayer

In consideration of the band inversion between p^{-}_{z} and p^{+}_{z}, it is possible to manipulate the electronic and topological properties of R–Bi bilayer *via* external electric field. When a downward vertical electric field ($E_{\perp}$) is applied, it is found that the degeneracy of energy band is lifted

because of the breaking of inversion symmetry, as shown in Fig. S6, and the magnitude of band splitting is proportional to the intensity of $E_\perp$. Under this circumstance, both VBM and CBM move close to the Fermi level with the increase of $E_\perp$, which leads to the continuous decrease of band gap, see Fig. 3(a). To understand such phenomenon, charge density distributions of CBM and VBM for the bilayer under the $E_\perp$ of –0.1 and –0.3 V/Å are plotted further, as depicted in Fig. S6. The result shows that the enhancement of $E_\perp$ makes the charge density of CBM more distributed in the interlayer Bi–Bi bonds, so the bonding state is strengthened and moves to low energy region, featured with the downshift of CBM. Similarly, the charge density distribution of VBM is boosted on the bilayer surface with increasing $E_\perp$, which results in a stronger antibonding state, and thus the VBM moves to high energy area. Figure S7 presents the corresponding edge states, in which the edge states arisen from the QSH effect are survived, but the edge states dominated by the TCI phase are gapped. It further demonstrates that the TCI phase is protected by ${\mathcal{G}_z}^a$ and ${\mathcal{G}_z}^b$, rather than $\mathcal{M}_x$, $\mathcal{M}_y$, $\mathcal{G}_x$, and $\mathcal{G}_y$, because among these mirror symmetry operations, only ${\mathcal{G}_z}^a$ and ${\mathcal{G}_z}^b$ can be broken by $E_\perp$. When the $E_\perp$ exceeds 0.45 V/Å, energy bands are intersected with the Fermi level, giving rise to electron and hole doping, see the inset in Fig. 3(a). In this instance, the R–Bi bilayer exhibits a metallic nature, and the bulk state becomes conductive, accompanied by the annihilation of dissipationless edge states. Additionally, it is necessary to point out that the above-mentioned phenomena can also be observed by the application of upward $E_\perp$ as a result of the inversion symmetry in R–Bi bilayer.

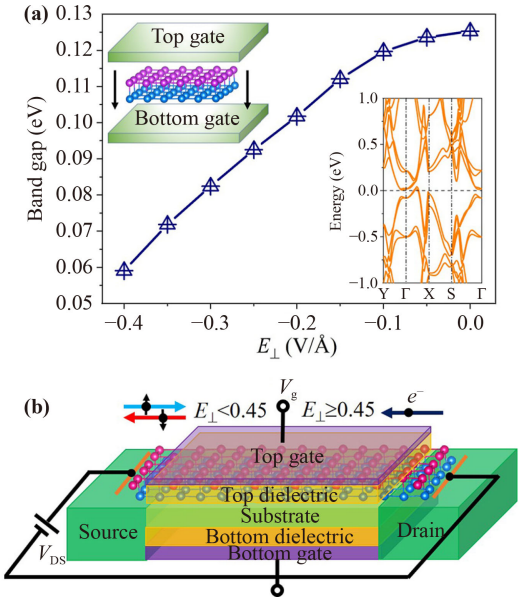

Fig. 3 **(a)** Variation of band gap as a function of $E_\perp$ for R–Bi bilayer. The upper and lower insets are schematic diagram of electric field applied to bilayer and SOC band structure of bilayer under the $E_\perp$ of –0.45 V/Å, respectively. **(b)** Prototype of designed TFET based on R–Bi bilayer.

The electric-field-induced phase transition between QSH insulator and metal offers a possibility to achieve electrical control of spin and charge currents for R–Bi bilayer, which is very attractive for the application in TFET. Here, a dual gated TFET based on a vdW heterostructure composed of R–Bi bilayer and wide gap insulator is proposed, and the device prototype is sketched in Fig. 3(b). The top and bottom gates would provide a vertical electric field to achieve the on/off function. The MgO crystal can be adopted as the dielectric layer due to its sizable band gap and dielectric permittivity [45, 46]. Considering the relationship between critical electric field of phase transition and breakdown field of dielectric layer, the thickness of MgO layer should be at least 10 nm. When the intensity of electric field is below 0.45 V/Å, net spin currents are produced at the edges of channel layer, whereas the insulating bulk state makes charge current blocked. At this point, the spin (charge) current shows the "on (off)" state. As the electric field is larger than 0.45 V/Å, the edge states would be switched off and substituted by the charge current flowing through the entire R–Bi bilayer, implying that the charge (spin) current is switched to "on (off)" state. Compared with traditional FET, the proposed TFET shows great technical advantages, e.g., superior resistor-capacitor response time and dissipationless edge transport property.

3.4 vdW heterostructure constructed by R–Bi bilayer and KBr(110) surface

For TFET fabrication, it is also important to search for a suitable substrate to support the R–Bi bilayer since the topological property of film is generally annihilated by the strong hybridization between substrate and film, such as stanene and Bi (111) on Bi_2Te_3 [47–49]. Here, the KBr(110) surface is employed to construct vdW heterostcutrue with the R–Bi bilayer. The lattice mismatches along a and b directions are 1.68% and 2.77%, respectively. Figures 4(a) and (b) display the structural schematic diagram of vdW heterostructure. The interlayer distance is found to be 3.36 Å, and the binding energy is calculated to be –128.7 meV/Å^2, suggesting that the interaction between bilayer and substrate belongs to the typical vdW interaction. The SOC band structure of heterostructure is shown in Fig. 4(c), in which the electronic states near the Fermi level are primarily derived from the R–Bi bilayer. More remarkably, the characteristic of band inversion for the bilayer is preserved, and the band gap is enhanced to 148.1 meV due to the proximity effect. The topological nature of R–Bi bilayer in heterostructure is further checked by the edge state calculation, see Fig. S8. Owing to the substrate-induced breakings of ${\mathcal{G}_z}^a$ and ${\mathcal{G}_z}^b$,

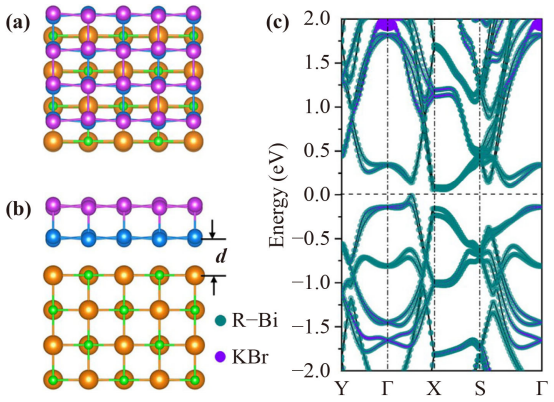

Fig. 4 **(a, b)** Top and side views of vdW heterostructure composed of R–Bi bilayer and KBr(110) surface. **(c)** Calculated SOC band structure of vdW heterostructure.

the edge states come from the TCI phase are vanished, while the edge states contributed by the TI phase are retained, indicating a favorable robustness of QSH effect for R–Bi bilayer, which has substantial implication for the application in TFET. To sustain and utilize the DTI phase of R–Bi, it is essential to construct a quantum-well structure that holds horizontal glide mirror symmetries, with the R–Bi bilayer sandwiched between two insulating layers.

3.5 Effect of strain on R–Bi bilayer

The relaxation strain is generally inevitable when depositing 2D crystal on substrate. In light of this, we explore the effect of strain on the electronic and topological properties of R–Bi bilayer. Considering the anisotropy of crystal structure of bilayer, the *a*-axial, *b*-axial and biaxial strains are employed, respectively. Figure 5(a) shows variations of energy levels [V_1, C_1, V_2 and C_2 in Fig. 1(e)] and band gap as a function of *a*-axial strain. One can see that both V_1 and C_2 move towards (away from) the Fermi level under the tensile (compressive) strain, and the V_2 shows an opposite change trend, while the variation of C_1 is complicated. Then the origin of change in energy levels is studied. Firstly, the charge density distributions of V_2 and C_2 are plotted, see Figs. S9(a) and (b), which are located at the Bi–Bi bond along the *a* direction, exhibiting the characteristics of bonding and antibonding states of $p_{x,y}$ orbitals, respectively. It is interesting to note that the thickness of bilayer is increased (decreased) when the *a*-axial compressive (tensile) strain is applied, as shown in Fig. S10. The

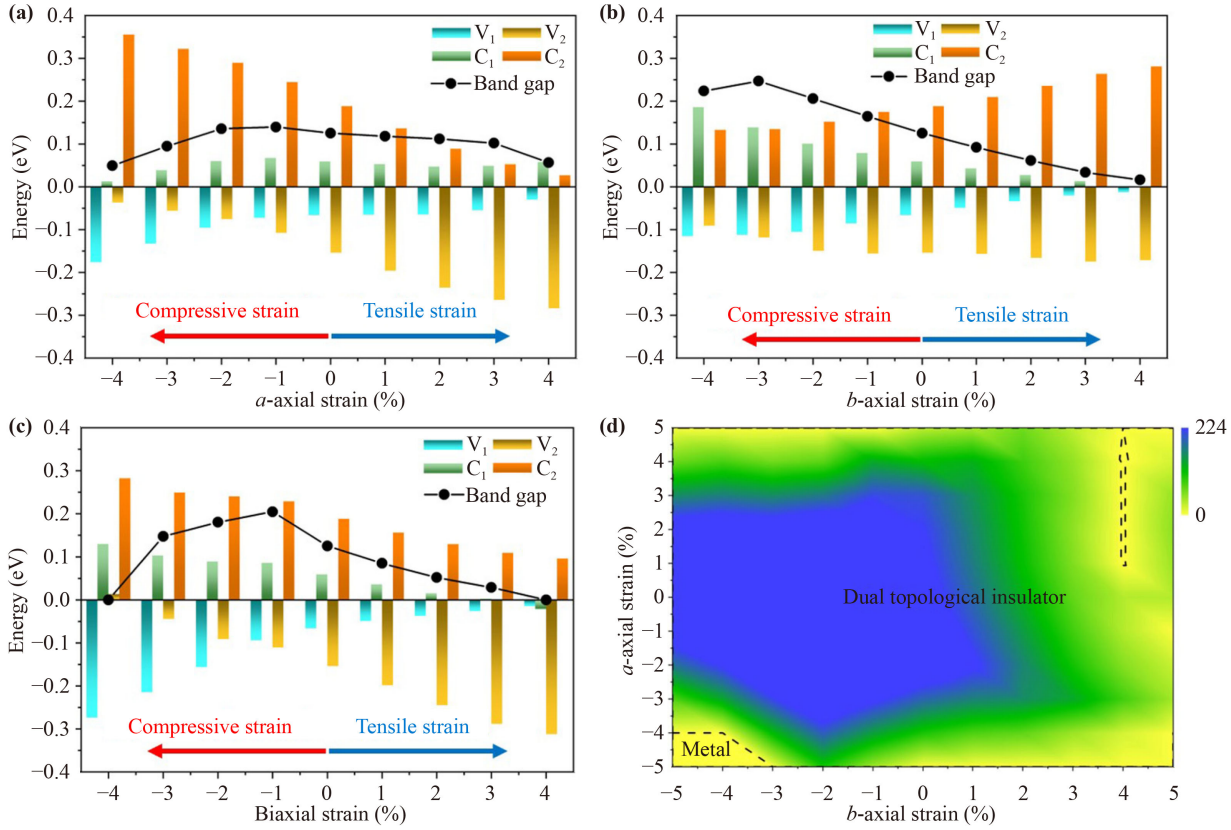

Fig. 5 **(a–c)** Variations of energy levels and band gap as a function of *a*-axial, *b*-axial, and biaxial strains, respectively. **(d)** Phase diagram of band gap for R–Bi bilayer under the dual regulation of *a*-axial and *b*-axial strains. The dotted line is the boundary of DTI and metal phases.

increased (decreased) thickness would weaken (enhance) the hybridization of p_z orbitals between upper and lower Bi atoms, which makes the corresponding electronic states more localized (extended). Hence, both V_1 and C_1 generally shift away from (towards) the Fermi level under compressive (tensile) strain. Furthermore, we also find that the bond angle θ is decreased (increased) with increasing compressive (tensile) strain, as depicted in Fig. S9(c). The θ is closely associated with the degree of hybridization of $p_{x,y}$ orbitals and Bi–Bi bond strength. The larger the θ is, the stronger the overlap between $p_{x,y}$ orbitals become, which would enhance the bonding state and weaken the antibonding state correspondingly. As a result, the tensile (compressive) strain drives both V_2 and C_2 to move to the low (high) energy region. Owing to the relative shift between energy levels, the transition between direct and indirect band gap can be observed in the process of applying *a*-axial strain. Meanwhile, the effective tunability of band gap is also achievable, in which the band gap can attain the maximum of 139.6 meV at –1% strain. As the *b*-axial strain is applied, the alteration of thickness of bilayer is analogous to the case of *a*-axial strain, as shown in Fig. S10, so the shift of V_1 and C_1 away from (toward) the Fermi level can be observed obviously under the compressive (tensile) strain, see Fig. 5(b). Notably, the variations of θ induced by *b*-axial and *a*-axial strains are diametrically opposite, and thus the evolutions of V_2 and C_2 under *b*-axial strain are roughly opposite to that of *a*-axial strain. Beyond that, the band gap can reach as large as 246.8 meV, and the direct band gap is preserved throughout the process except for the case of –3% strain. For the employment of biaxial strain, the variations of V_1 and C_1 are consistent with the previous two types of strains because of the same mechanism, see Fig. S10. The V_2 and C_2 show a similar trend to the case of *a*-axial strain, which may be attributed to that the *a*-axial strain is directly responsible for the Bi–Bi bond strength in the *a* direction. The band gap can be enlarged to 204.6 meV at –1% strain, but it would drop to zero when the tensile (compressive) strain is larger than 4% due to the emergence of self-doping, as illustrated in Fig. 5(c). In a word, the topologically nontrivial phase of R–Bi bilayer shows a favorable robustness against strain, and the magnitude of band gap can be effectively modulated. In reality, the substrate-induced relaxation strain is generally complicated, which cannot be simply described by above conditions, such as R–Bi bilayer deposited on KBr(110) surface. Therefore, we expand our investigation to the effect of combinatorial regulation of *a*-axial and *b*-axial strains on the R–Bi bilayer. Figure 5(d) presents the phase diagram of band gap, from which we find that the nontrivial topology of R–Bi bilayer is maintained over a wide range of strain. The self-doping-induced metallic property would occur when both *a*-axial and *b*-axial compressive strains are sufficiently large. Remarkably, the band gap is raised in varying degrees, which provides certain guidance for the experimental observation of topological phases for R–Bi bilayer.

4 Conclusion

In summary, using first-principles calculations, we propose a new 2D DTI, i.e., R–Bi bilayer, which simultaneously possesses TI and TCI phases with a nontrivial band gap of 125.3 meV. Such topological state is confirmed by band inversion, nonzero $\mathbb{Z}_2$ topological invariant and mirror Chern numbers, as well as edge states across the bulk band gap. The TCI phase in R–Bi bilayer is protected by horizontal glide mirror symmetries, instead of traditional mirror symmetry. The bulk band gap can be effectively manipulated by external electric field and strains. Moreover, the electric field can bring about the transition between TI and metallic phases for the R–Bi bilayer, and a TFET is proposed based on this feature, which aims to rapidly control the spin and charge carriers. The KBr(110) surface is demonstrated as a suitable substrate for supporting the R–Bi bilayer, without affecting its QSH effect. Our works pave the way to explore DTI phase related to the glide mirror symmetry, and provide an excellent material platform for practical applications in spintronics.

Declaration of competing interest The authors declare that they have no known competing financial interests or personal relationships that could have influenced the work reported in this paper.

Electronic supplementary materials The online version contains supplementary material available at https://doi.org/10.1007/10.1007/s11467-023-1262-x and https://journal.hep.com.cn/fop/EN/10.1007/s11467-023-1262-x.

Acknowledgements This work was supported by the National Natural Science Foundation of China (Grant No. 12004137), the Taishan Scholar Project of Shandong Province (No. ts20190939), and the Natural Science Foundation of Shandong Province (Grant No. ZR2020QA052).

References

1. J. E. Moore, The birth of topological insulators, *Nature* 464(7286), 194 (2010)
2. M. Z. Hasan and C. L. Kane, Colloquium: Topological insulators, *Rev. Mod. Phys.* 82(4), 3045 (2010)
3. L. Fu, Topological crystalline insulators, *Phys. Rev. Lett.* 106(10), 106802 (2011)
4. Y. Ando, Topological insulator materials, *J. Phys. Soc. Jpn.* 82(10), 102001 (2013)
5. Y. Ando and L. Fu, Topological crystalline insulators and topological superconductors: From concepts to materials, *Annu. Rev. Condens. Matter Phys.* 6(1), 361 (2015)
6. C. Niu, P. M. Buhl, G. Bihlmayer, D. Wortmann, Y.

Dai, S. Blügel, and Y. Mokrousov, Robust dual topological character with spin-valley polarization in a monolayer of the Dirac semimetal Na_3Bi, *Phys. Rev. B* 95(7), 075404 (2017)
7. N. Mao, X. Hu, C. Niu, B. Huang, and Y. Dai, Dual topological insulator and insulator–semimetal transition in mirror-symmetric honeycomb materials, *Phys. Rev. B* 100(20), 205116 (2019)
8. N. Avraham, A. Kumar Nayak, A. Steinbok, A. Norris, H. Fu, Y. Sun, Y. Qi, L. Pan, A. Isaeva, A. Zeugner, C. Felser, B. Yan, and H. Beidenkopf, Visualizing coexisting surface states in the weak and crystalline topological insulator Bi_2TeI, *Nat. Mater.* 19(6), 610 (2020)
9. I. Cucchi, A. Marrazzo, E. Cappelli, S. Riccò, F. Y. Bruno, S. Lisi, M. Hoesch, T. K. Kim, C. Cacho, C. Besnard, E. Giannini, N. Marzari, M. Gibertini, F. Baumberger, and A. Tamai, Bulk and surface electronic structure of the dual-topology semimetal Pt_2HgSe_3, *Phys. Rev. Lett.* 124(10), 106402 (2020)
10. M. Eschbach, M. Lanius, C. Niu, E. Młyńczak, P. Gospodarič, J. Kellner, P. Schüffelgen, M. Gehlmann, S. Döring, E. Neumann, M. Luysberg, G. Mussler, L. Plucinski, M. Morgenstern, D. Grützmacher, G. Bihlmayer, S. Blügel, and C. M. Schneider, Bi_1Te_1 is a dual topological insulator, *Nat. Commun.* 8(1), 14976 (2017)
11. J. I. Facio, S. K. Das, Y. Zhang, K. Koepernik, J. van den Brink, and I. C. Fulga, Dual topology in jacutingaite Pt_2HgSe_3, *Phys. Rev. Mater.* 3(7), 074202 (2019)
12. H. Lee, Y. G. Kang, M. C. Jung, M. J. Han, and K. J. Chang, Robust dual topological insulator phase in NaZnBi, *NPG Asia Mater.* 14(1), 36 (2022)
13. I. Matsuda, K. Yaji, A. A. Taskin, M. D'angelo, R. Yukawa, Y. Ohtsubo, P. Le Fèvre, F. Bertran, S. Yoshizawa, A. Taleb-Ibrahimi, A. Kakizaki, Y. Ando, and F. Komori, Surface state of the dual topological insulator $Bi_{0.91}Sb_{0.09}(11\bar{2})$, *Physica B* 516, 100 (2017)
14. T. Rauch, M. Flieger, J. Henk, I. Mertig, and A. Ernst, Dual topological character of chalcogenides: Theory for Bi_2Te_3, *Phys. Rev. Lett.* 112(1), 016802 (2014)
15. J. C. Y. Teo, L. Fu, and C. L. Kane, Surface states and topological invariants in three-dimensional topological insulators: Application to $Bi_{1-x}Sb_x$, *Phys. Rev. B* 78(4), 045426 (2008)
16. C. Fang and L. Fu, New classes of three-dimensional topological crystalline insulators: Nonsymmorphic and magnetic, *Phys. Rev. B* 91(16), 161105 (2015)
17. H. Kim and S. Murakami, Glide-symmetric topological crystalline insulator phase in a nonprimitive lattice, *Phys. Rev. B* 102(19), 195202 (2020)
18. J. Ma, C. Yi, B. Lv, Z. J. Wang, S. Nie, L. Wang, L. Kong, Y. Huang, P. Richard, P. Zhang, K. Yaji, K. Kuroda, S. Shin, H. Weng, B. A. Bernevig, Y. Shi, T. Qian, and H. Ding, Experimental evidence of hourglass fermion in the candidate nonsymmorphic topological insulator KHgSb, *Sci. Adv.* 3(5), e1602415 (2017)
19. Z. Wang, A. Alexandradinata, R. J. Cava, and B. A. Bernevig, Hourglass fermions, *Nature* 532(7598), 189 (2016)
20. Y. L. Chen, M. Kanou, Z. K. Liu, H. J. Zhang, J. A. Sobota, D. Leuenberger, S. K. Mo, B. Zhou, S. L. Yang, P. S. Kirchmann, D. H. Lu, R. G. Moore, Z. Hussain, Z. X. Shen, X. L. Qi, and T. Sasagawa, Discovery of a single topological Dirac fermion in the strong inversion asymmetric compound BiTeCl, *Nat. Phys.* 9(11), 704 (2013)
21. B. Yan, M. Jansen, and C. Felser, A large-energy-gap oxide topological insulator based on the superconductor $BaBiO_3$, *Nat. Phys.* 9(11), 709 (2013)
22. H. Zhang, C. X. Liu, X. L. Qi, X. Dai, Z. Fang, and S. C. Zhang, Topological insulators in Bi_2Se_3, Bi_2Te_3 and Sb_2Te_3 with a single Dirac cone on the surface, *Nat. Phys.* 5(6), 438 (2009)
23. M. M. Otrokov, I. I. Klimovskikh, H. Bentmann, D. Estyunin, A. Zeugner, Z. S. Aliev, S. Gaß, A. U. B. Wolter, A. V. Koroleva, A. M. Shikin, M. Blanco-Rey, M. Hoffmann, I. P. Rusinov, A. Y. Vyazovskaya, S. V. Eremeev, Y. M. Koroteev, V. M. Kuznetsov, F. Freyse, J. Sánchez-Barriga, I. R. Amiraslanov, M. B. Babanly, N. T. Mamedov, N. A. Abdullayev, V. N. Zverev, A. Alfonsov, V. Kataev, B. Büchner, E. F. Schwier, S. Kumar, A. Kimura, L. Petaccia, G. Di Santo, R. C. Vidal, S. Schatz, K. Kißner, M. Ünzelmann, C. H. Min, S. Moser, T. R. F. Peixoto, F. Reinert, A. Ernst, P. M. Echenique, A. Isaeva, and E. V. Chulkov, Prediction and observation of an antiferromagnetic topological insulator, *Nature* 576(7787), 416 (2019)
24. C. Z. Chang, J. Zhang, X. Feng, J. Shen, Z. Zhang, M. Guo, K. Li, Y. Ou, P. Wei, L. L. Wang, Z. Q. Ji, Y. Feng, S. Ji, X. Chen, J. Jia, X. Dai, Z. Fang, S. C. Zhang, K. He, Y. Wang, L. Lu, X. C. Ma, and Q. K. Xue, Experimental observation of the quantum anomalous Hall effect in a magnetic topological insulator, *Science* 340(6129), 167 (2013)
25. F. Reis, G. Li, L. Dudy, M. Bauernfeind, S. Glass, W. Hanke, R. Thomale, J. Schäfer, and R. Claessen, Bismuthene on a SiC substrate: A candidate for a high-temperature quantum spin Hall material, *Science* 357(6348), 287 (2017)
26. Y. Lu, W. Xu, M. Zeng, G. Yao, L. Shen, M. Yang, Z. Luo, F. Pan, K. Wu, T. Das, P. He, J. Jiang, J. Martin, Y. P. Feng, H. Lin, and X. Wang, Topological properties determined by atomic buckling in self-assembled ultrathin Bi(110), *Nano Lett.* 15(1), 80 (2015)
27. Y. Bai, L. Cai, N. Mao, R. Li, Y. Dai, B. Huang, and C. Niu, Doubled quantum spin Hall effect with high-spin Chern number in α-antimonene and α-bismuthene, *Phys. Rev. B* 105(19), 195142 (2022)
28. L. Kou, X. Tan, Y. Ma, H. Tahini, L. Zhou, Z. Sun, D. Aijun, C. Chen, and S. C. Smith, Tetragonal bismuth bilayer: A stable and robust quantum spin Hall insulator, *2D Mater.* 2, 045010 (2015)
29. R. W. Zhang, C. W. Zhang, W. X. Ji, S. S. Yan, and Y. G. Yao, First-principles prediction on bismuthylene monolayer as a promising quantum spin Hall insulator, *Nanoscale* 9(24), 8207 (2017)
30. X. Kong, L. Li, O. Leenaerts, X. J. Liu, and F. M. Peeters, New group-V elemental bilayers: A tunable structure model with four-, six-, and eight-atom rings, *Phys. Rev. B* 96(3), 035123 (2017)
31. G. Kresse and J. Furthmüller, Efficient iterative schemes for *ab initio* total-energy calculations using a

plane-wave basis set, *Phys. Rev. B* 54(16), 11169 (1996)
32. G. Kresse and J. Hafner, *Ab initio* molecular-dynamics simulation of the liquid-metal–amorphous-semiconductor transition in germanium, *Phys. Rev. B* 49(20), 14251 (1994)
33. G. Kresse and D. Joubert, From ultrasoft pseudopotentials to the projector augmented-wave method, *Phys. Rev. B* 59(3), 1758 (1999)
34. S. Grimme, Semiempirical GGA-type density functional constructed with a long-range dispersion correction, *J. Comput. Chem.* 27(15), 1787 (2006)
35. J. P. Perdew and Y. Wang, Accurate and simple analytic representation of the electron-gas correlation energy, *Phys. Rev. B* 45(23), 13244 (1992)
36. S. Grimme, J. Antony, S. Ehrlich, and H. Krieg, A consistent and accurate *ab initio* parametrization of density functional dispersion correction (DFT-D) for the 94 elements H–Pu, *J. Chem. Phys.* 132(15), 154104 (2010)
37. S. Grimme, S. Ehrlich, and L. Goerigk, Effect of the damping function in dispersion corrected density functional theory, *J. Comput. Chem.* 32(7), 1456 (2011)
38. A. A. Soluyanov and D. Vanderbilt, Wannier representation of Z_2 topological insulators, *Phys. Rev. B* 83(3), 035108 (2011)
39. A. A. Soluyanov and D. Vanderbilt, Computing topological invariants without inversion symmetry, *Phys. Rev. B* 83(23), 235401 (2011)
40. M. P. L. Sancho, J. M. L. Sancho, and J. Rubio, Quick iterative scheme for the calculation of transfer matrices: Application to Mo(100), *J. Phys. F Met. Phys.* 14(5), 1205 (1984)
41. M. P. L. Sancho, J. M. L. Sancho, J. M. L. Sancho, and J. Rubio, Highly convergent schemes for the calculation of bulk and surface Green functions, *J. Phys. F Met. Phys.* 15(4), 851 (1985)
42. J. Liu, T. H. Hsieh, P. Wei, W. Duan, J. Moodera, and L. Fu, Spin-filtered edge states with an electrically tunable gap in a two-dimensional topological crystalline insulator, *Nat. Mater.* 13(2), 178 (2014)
43. J. Liu, X. Qian, and L. Fu, Crystal field effect induced topological crystalline insulators in monolayer IV–VI semiconductors, *Nano Lett.* 15(4), 2657 (2015)
44. C. Niu, P. M. Buhl, G. Bihlmayer, D. Wortmann, S. Blügel, and Y. Mokrousov, Topological crystalline insulator and quantum anomalous Hall states in IV-VI-based monolayers and their quantum wells, *Phys. Rev. B* 91(20), 201401 (2015)
45. L. Yan, C. M. Lopez, R. P. Shrestha, E. A. Irene, A. A. Suvorova, and M. Saunders, Magnesium oxide as a candidate high-κ gate dielectric, *Appl. Phys. Lett.* 88(14), 142901 (2006)
46. A. Posadas, F. J. Walker, C. H. Ahn, T. L. Goodrich, Z. Cai, and K. S. Ziemer, Epitaxial MgO as an alternative gate dielectric for SiC transistor applications, *Appl. Phys. Lett.* 92(23), 233511 (2008)
47. T. Hirahara, G. Bihlmayer, Y. Sakamoto, M. Yamada, H. Miyazaki, S. I. Kimura, S. Blügel, and S. Hasegawa, Interfacing 2D and 3D topological insulators: Bi(111) bilayer on Bi_2Te_2, *Phys. Rev. Lett.* 107(16), 166801 (2011)
48. F. Yang, L. Miao, Z. F. Wang, M. Y. Yao, F. Zhu, Y. R. Song, M. X. Wang, J. P. Xu, A. V. Fedorov, Z. Sun, G. B. Zhang, C. Liu, F. Liu, D. Qian, C. L. Gao, and J. F. Jia, Spatial and energy distribution of topological edge states in single Bi(111) bilayer, *Phys. Rev. Lett.* 109(1), 016801 (2012)
49. F. Zhu, W. Chen, Y. Xu, C. Gao, D. Guan, C. Liu, D. Qian, S. C. Zhang, and J. Jia, Epitaxial growth of two-dimensional stanene, *Nat. Mater.* 14(10), 1020 (2015)